Development of a Parametric Model of Adult Human Ear Geometry

Matthew P. Reed
Anne Bonifas

Biosciences Group
University of Michigan Transportation Research Institute

UMTRI-2023-7

May 2023

Development of a Parametric Model of Adult Human Ear Geometry

Final Report

by

Matthew P. Reed
Anne Bonifas

University of Michigan Transportation Research Institute

UMTRI-2023-7

May 2023

REPORT DOCUMENTATION PAGE

Form Approved
OMB No. 0704-0188

1. REPORT DATE *(DD-MM-YYYY)*	**2. REPORT TYPE**	**3. DATES COVERED** *(From - To)*
April 30, 2023	Final Report	

4. TITLE AND SUBTITLE

Development of a Parametric Model of Adult Human Ear Geometry

5a. CONTRACT NUMBER

5b. GRANT NUMBER

5c. PROGRAM ELEMENT NUMBER

6. AUTHOR(S)

Reed, Matthew P. and Bonifas, Anne

5d. PROJECT NUMBER

5e. TASK NUMBER

5f. WORK UNIT NUMBER

7. PERFORMING ORGANIZATION NAME(S) AND ADDRESS(ES)

University of Michigan
Transportation Research Institute

8. PERFORMING ORGANIZATION REPORT

UMTRI-2023-7

9. SPONSORING / MONITORING AGENCY NAME(S) AND ADDRESS(ES)

Amazon

10. SPONSOR/MONITOR'S ACRONYM(S)

11. SPONSOR/MONITOR'S REPORT NUMBER(S)

Issued Upon Submission

12. DISTRIBUTION / AVAILABILITY STATEMENT

13. SUPPLEMENTARY NOTES

14. ABSTRACT

Quantitative knowledge regarding the size and shape of the human ear is valuable for the design of hearing protection and audio devices. Prior studies have used primarily landmark-to-landmark measurements rather than a three-dimensional analysis. To address the need for a parametric, high-resolution, three-dimensional model of adult ear geometry, a retrospective analysis of computed tomography (CT) scans from a patient database was conducted. The geometry of the pinna, canal, and adjacent scalp was extracted in skull-based coordinates for 331 ears from 224 men and women ages 18 to 81 years. A template polygonal mesh with 60040 vertices was fit to the geometry with a median distance error across ears of 0.03 mm and a median 99.9^{th} percentile distance error of 0.44 mm. Principal component analysis demonstrated a large amount of variance not previously quantified in the position and orientation of the ears with respect to the skull. A regression analysis confirmed previous findings of sex differences in the increase of ear size with increasing age and also demonstrated an effect of body mass index on ear position and orientation that has not been previously described. A boundary method in principal component space was used to generate a set of ears suitable for designing devices for which the ear position on the head is important. Boundary ears were also generated in pinna-centered coordinates for applicability to in-ear device design, demonstrating the flexibility of the dataset and analysis methodology. To our knowledge, this study developed the largest and highest-resolution database of human ear geometry, the first to be measured in head-centered coordinates, and the first to include the geometry of the canal to the ear drum. Future work is needed to extend the applicability to populations not well represented in the current database.

15. SUBJECT TERMS
Human, Ear, Geometry, Anthropometry

16. SECURITY CLASSIFICATION OF:			**17. LIMITATION OF ABSTRACT**	**18. NUMBER OF PAGES**	**19a. NAME OF RESPONSIBLE PERSON M.P. Reed**
a. REPORT UNCLASSIFIED, Dist A.	**b. ABSTRACT** UNCLASSIFIED, Dist A.	**c. THIS PAGE** UNCLASSIFIED, Dist A.		33	**19b. TELEPHONE NUMBER** *(include area code)* (734) 936-1111

ACKNOWLEDGMENTS

This work was supported by Amazon. We thank our collaborators at Amazon, including Mihir Shetye and Alex Epstein. At UMTRI, several students contributed to the data extraction and processing, including Alec Murrell, Samarth Kadambi, and Wuyuqing Yang. Special thanks to Tyler Vallier, who developed extraction methods, including the method for identifying the eardrum, and who meticulously digitized the landmarks on all scans.

CONTENTS

ABSTRACT

Quantitative knowledge regarding the size and shape of the human ear is valuable for the design of hearing protection and audio devices. Prior studies have used primarily landmark-to-landmark measurements rather than a three-dimensional analysis. To address the need for a parametric, high-resolution, three-dimensional model of adult ear geometry, a retrospective analysis of computed tomography (CT) scans from a patient database was conducted. The geometry of the pinna, canal, and adjacent scalp was extracted in skull-based coordinates for 331 ears from 224 men and women ages 18 to 81 years. A template polygonal mesh with 60040 vertices was fit to the geometry with a median distance error across ears of 0.03 mm and a median 99.9th percentile distance error of 0.44 mm. Principal component analysis demonstrated a large amount of variance not previously quantified in the position and orientation of the ears with respect to the skull. A regression analysis confirmed previous findings of sex differences in the increase of ear size with increasing age and demonstrated an effect of body mass index on ear position and orientation that has not been previously described. A boundary method in principal component space was used to generate a set of ears suitable for designing devices for which the ear position on the head is important. Boundary ears were also generated in pinna-centered coordinates for applicability to in-ear device design, demonstrating the flexibility of the dataset and analysis methodology. To our knowledge, this study developed the largest and highest-resolution database of human ear geometry, the first to be measured in head-centered coordinates, and the first to include the geometry of the canal to the ear drum. Future work is needed to extend the applicability to populations not well represented in the current database.

INTRODUCTION

The size and shape of the human ear has been studied extensively (Farkas 1978, Alexander et al. 2011, Fu and Luximon 2020). The ear exhibits complex, visible geometry that varies enough across individuals that it has been proposed as a biometric identifier (Cintas et al. 2017, Koboj et al. 2020). The size, shape, and location of the ear are critical inputs to the design of hearing protection and both in-ear and head-worn audio devices, including headphones, earbuds, and hearing aids (Liu 2008, Ji et al. 2018, Lu et al. 2021). The size and shape of the ear affects the head-related transfer function (HRTF), which affects the ability of the listener to localize sound (Pollack et al. 2020).

Due to the variability of individual ears, hearing protection and hearing aids are often designed from molds made of the user's ear. Molding material is pressed into the canal and adjacent concha areas to capture the shape, then carefully removed and scanned to produce custom in-ear devices. Experienced audiologists are able to use the measured geometry to produce comfortable and effective devices that remain in place. Statistical modeling of ear molds has been conducted to characterize the distribution of ear shape in this important area (Paulsen et al. 2002; Baloch et al. 2010).

In spite of the importance of ear geometry for design applications, most prior studies of the whole pinna have reported linear dimensions between landmarks (Farkas 1978, Niemitz et al. 2007, Sforza et al. 2009, Alexander et al. 2011). Although this information is useful for comparing ear dimensions across populations, it is difficult to apply to the design of three-dimensional (3D) products. In recent years, improvements in measurement and analysis methods have enabled 3D modeling of a large range of complex body structures, from faces to fingers and toes. However, few papers describe detailed 3D models of the ear. Several studies have used morphable template models to fit the geometry of the pinna (Chu et al. 2019, Fantini et al. 2021).

Two recent studies have integrated 3D surface scans of the ear with scans of molds taken of the concha and outer canal. Lee et al. (2018) reported a large number of linear dimensions based on manual digitization of scan data from 230 Koreans and 96 Caucasians. Fan et al. (2021a, 2021b) obtained surface scans and canal molds from the left and right ears of 700 Chinese adults. Summary statistics on a large number of dimensions of the pinna outer canal were reported. However, neither of these recent studies reported the generation of an integrated statistical model of ear shape.

This report describes the development of a parametric model of the adult human ear based on geometry extracted from computed tomography (CT) scans taken as part of medical care. CT scanners obtain detailed images of structures in the body by rotating an x-ray head and detector around the patient's body. The geometry of anatomical components can be extracted from these images by specifying a range of density (attenuation) corresponding to the desired tissue (for example, skin or bone). CT scans have been used in prior research relating to the middle and inner ear (Fernanda et al. 2014), but do not appear to have been used to quantify the geometry of the pinna and canal. For the current study, CT scans were obtained retrospectively from a patient database and de-identified under approval of an Institutional Review Board.

Skin surface data that included the detailed ear geometry from the scalp and pinna through the canal to the middle ear were extracted along with the skull from a convenience sample of scans from 224 men and women ages 18 to 81 years. A total of 331 ears were extracted after aligning each head to a common coordinate system. The number of ears extracted was smaller than twice the number of subjects due to distortions of one ear for some subjects due to the supports used to position the subject's head during the scan. Using custom software and a semi-automated technique, a polygonal template with 60k vertices was fit to each ear. Principal component analysis (PCA) and regression were used to explore the primary modes of size and shape variance along with the associations with covariates such as sex and age. The resulting dataset and model have broad applicability to ear-related design problems.

METHODS

Obtaining Medical Imaging Studies

De-identified CT studies were obtained from the radiology archives at the University of Michigan Medical Center using protocols approved by a U-M Institutional Review Board (HUM00004842). The patient age, sex, stature (erect standing height), and body weight were obtained for each study. Data were gathered from scanning protocols with the patient prone (face down) or supine (face up). Due to the action of gravity on the tissues, the data from these poses are slightly different, so these effects were assessed statistically. The resolution of the CT images was 0.625 mm between slices and in-plane resolution of 0.7 to 1 mm for the prone studies and 0.3 to 0.5 mm for the supine studies.

Subjects

Table 1 shows summary statistics for the covariates of the 224 subjects. An effort was made to obtain approximately equal numbers of male and female subjects well distributed across the adult age range, but otherwise this is a convenience sample. Two ears were obtained from 107 subjects while the remaining subjects contributed a single ear, due to problems with the contralateral ear such as deformation of the pinna due to head supports used during scanning. A total of 155 ears were obtained from prone scans and 176 from supine.

Table 1A
Male Age and Body Dimensions: 160 ears; 83 Right, 92 Left

Male	Min	Median	Max
Stature (mm)	1658 (65”)	1778 (70”)	1981 (78”)
BMI (kg/m^2)	19.1	36.6	42.2
Age (yr)	18.0	43.0	81

Table 1B
Female Age and Body Dimensions: 171 ears; 79 Right, 92 Left

Female	Min	Median	Max
Stature (mm)	1461 (58”)	1626 (64”)	1854 (73”)
BMI (kg/m^2)	14.8	26.0	48.0
Age (yr)	19.0	42.0	79

Extracting Skull and Skin Surfaces

After verifying that the ears did not exhibit any anomalies, such as modifications beyond typical piercings or overt pathological changes, the geometry of the skin of the head was extracted using semi-automated methods in Mimics software

(https://www.materialise.com/). The skin surface was extracted using a window of -325 to 200 HU Hounsfield units (HU), which was manually adjusted as needed to obtain a clean representation of the skin surface. The surfaces of the sinuses and other areas within the head that were not of interest were manually removed. The skull was extracted using a standard bone thresholding window of 226 to 3071 HU.

Aligning and Extracting Ears

The locations of the left and right porion and infraorbitale landmarks, which together define the Frankfurt plane, were digitized on each skull (Figure 1). The porion lies at the superior margin of the external auditory meatus in the temporal bone, and the infraorbitale landmark is the lowest point on the inferior margin of the orbit. All of the skull landmarks were digitized by the same person. Landmarks were digitized three times on a randomly selected set of 10 skulls to quantify repeatability. The median (across subjects) of the median landmark discrepancy was 0.40 mm. That is, half of the measured landmark locations were less than 0.4 mm from the mean value obtained from three measurements. The median (across subjects) 95th percentile landmark discrepancy was 0.83 mm. The root-mean-square (RMS) discrepancy across all ears and landmarks was 0.89 mm, and the 95th percentile RMS value was 1.7 mm.

The head was aligned to a right-handed coordinate system with the origin located at the midpoint between the porion landmarks, the Y axis passing through both porion landmarks and positive to the left, X axis positive forward, and the Z axis positive upward. Thus, the ear geometry analysis was conducted in a head-centered coordinate system, rather than local to the ear. The left ears were mirrored to the right side around the XZ plane to facilitate analysis.

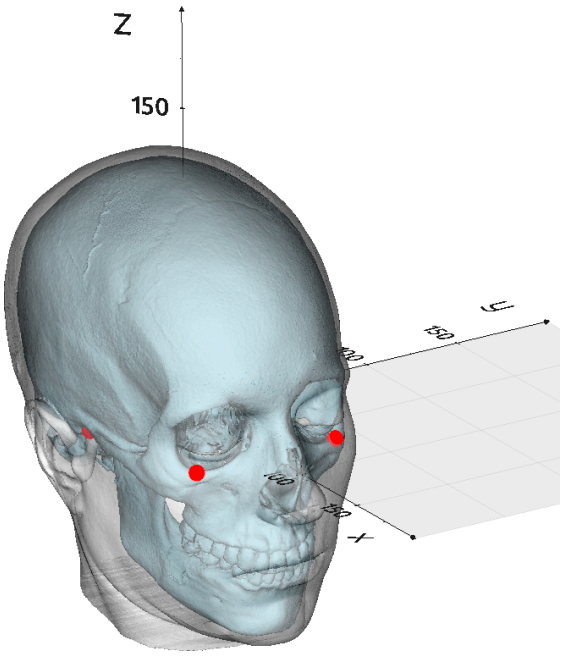

Figure 1. Head-centered coordinate system based on porion and infraorbitale landmarks (red spheres).

The ear area including the adjacent scalp was automatically extracted after head alignment (Figure 2). The middle ear geometry was then manually removed at the estimated location of the tympanic membrane (ear drum). In the supine scans with 0.625-mm resolution, the ossicles (middle ear bones) could be visualized on some of the scans, enabling the ear drum location to be estimated within about 1 mm. Based on review of several dozen scans, the typical location of the ear drum with respect to the exterior geometry of the middle ear was determined. This information was then used in a manual process to remove the middle ear geometry and cap the canal at the estimated ear drum location.

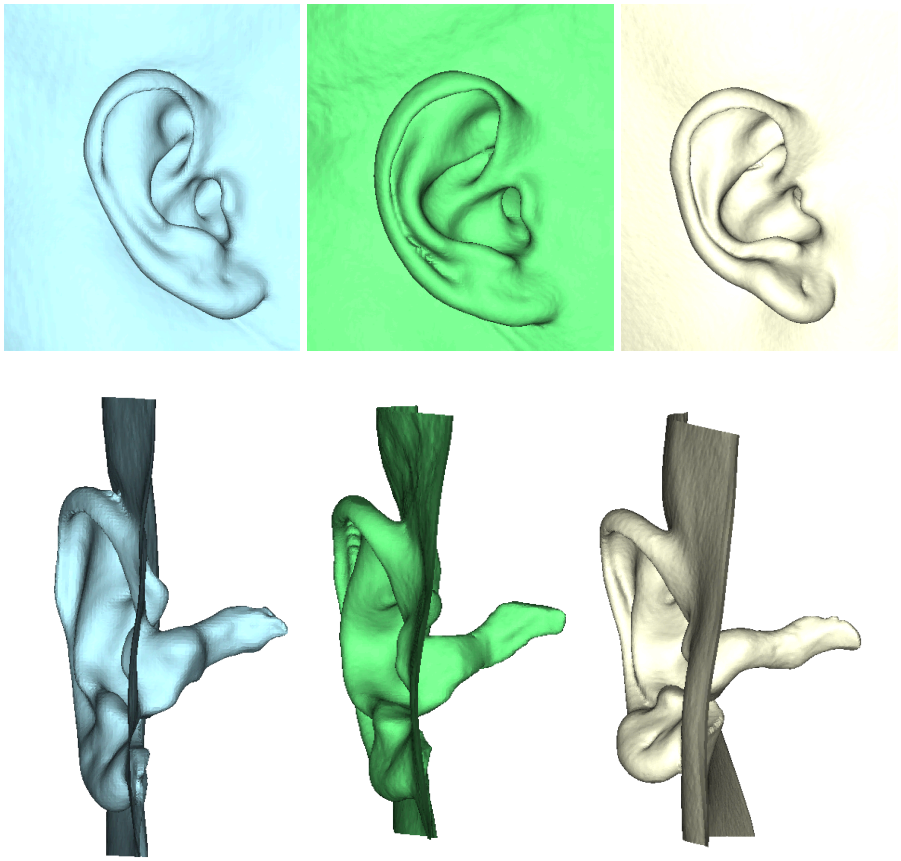

Figure 2. Example ears extracted from CT in lateral view (top) and front view (bottom).

Manual Landmark Digitization

To aid in analysis of the ear geometry, a set of landmarks were manually located on each ear. Figure 3 shows the landmarks. The landmarks were chosen to facilitate template fitting and to maximize homology in certain areas, rather than to match landmarks used in prior studies. For example, points on the helix were matched with points on the back of the pinna to facilitate template fitting. All of the landmarks were digitized by the same person. Landmarks were digitized three times on a randomly selected set of 10 ears to quantify repeatability. Landmarking discrepancies were expressed as the 3D distance of the measured landmark location from the mean for that landmark on that ear. The median (across ears) of the median landmark discrepancy was 0.34 mm. That is, half of the

measured landmark locations were less than 0.4 mm from the mean value obtained from three measurements. The median (across ears) 95th percentile landmark discrepancy was 1.2 mm. The root-mean-square (RMS) discrepancy across all ears and landmarks was 0.73 mm, and the 95th percentile RMS value was 1.9 mm. Relative to the mean pinna height of 56 mm, these values represent 1.2% and 3.3%, respectively.

Fitting Homologous Mesh

To enable statistical shape analysis, a polygonal template mesh was fit to each ear. The template was generated by a bootstrapping procedure that involved fitting a subset of data, computing the mean, then refitting the data with the mean ear geometry. Experimentation with tradeoffs between mesh resolution and fitting time and fitting quality led to the selection of a template mesh with 60040 vertices and 119655 triangles.

The template mesh was fitted to the ear geometry in a multistep process using openly available libraries as well as custom software written in Python for this application making extensive use of the *vedo* wrapper for the *vtk* library (Musy 2023, Schroeder et al. 2006). First, the extracted ear geometry was smoothed by using the Poisson reconstruction filter from the *pymeshlab* library (Muntoni and Cignoni 2021) with the *pointweight* parameter set to 4. Reconstructing the surface improved the consistency of normals and addressed a problem in which vertices from both sides of the skin were interposed, resulting in a jagged surface. The reconstructed mesh typically had 120k vertices and 240k polygons. The median across ears of the median distances between the original and reconstructed meshes was 0.008 mm; the 95th percentile median was 0.018 mm. The median 99.9th percentile distance was 0.18 mm.

In addition to the manually digitized landmarks, a set of landmarks were automatedly generated in the canal and on the perimeter of the scalp section (Figure 3). The goal of the canal landmarking procedure was to ensure a high level of homology in the canal fitting, in spite of the canal lacking well-defined landmarks. Using custom software, a process similar to the median axis transform was used to place points along the approximate centerline of the canal, starting just medial to the ear drum. The algorithm generated the largest sphere that would fit within the canal at the current Y-axis location, then stepped outward repeating the process out to the Y plane of the tragion landmark. A cubic interpolating spline was constructed connecting the centers of the spheres, and this spline was sampled at 15 evenly spaced points to obtain the canal landmark set. The perimeter points were generated in two rows along all four edges of the scalp boundary.

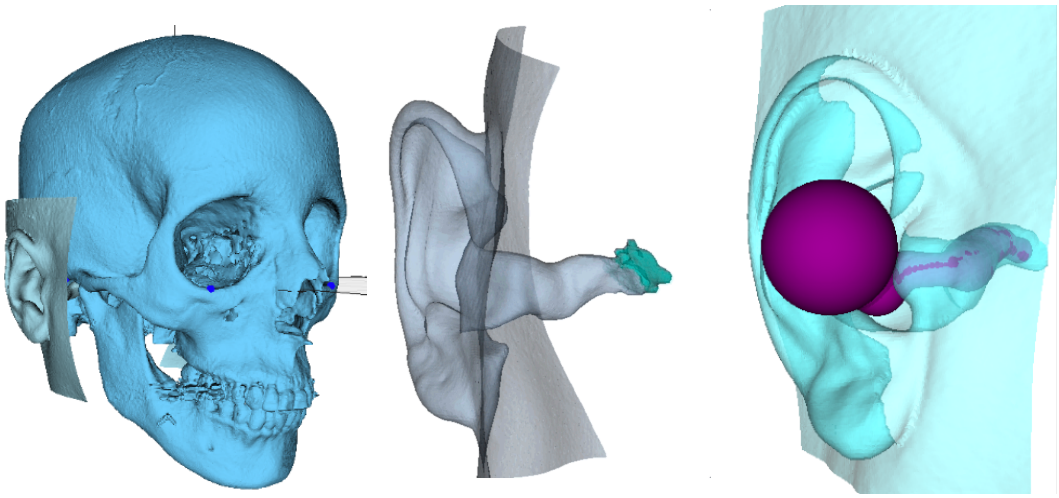

Figure 3. Illustration of steps in the data processing pipeline: (a) extracting the ear geometry in skull coordinates, (b) removing the middle ear at the estimated eardrum location, and (c) estimating the centerline of the canal by sphere fitting and splining.

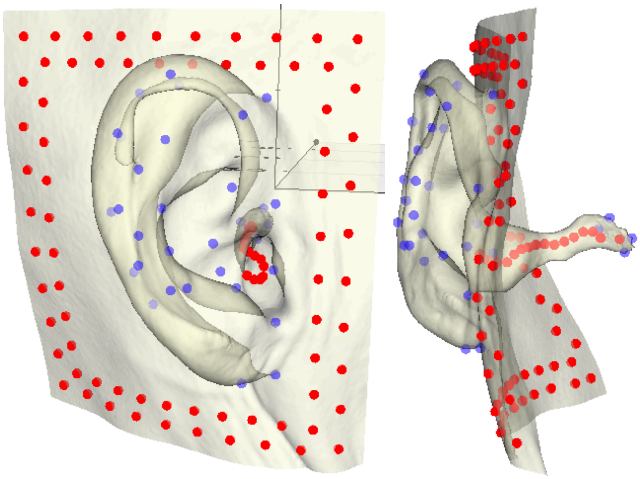

Figure 4. Manual (blue) and automatically generated (red) landmarks.

An initial non-rigid landmark-to-landmark morph was performed using a radial-basis-function (RBF) interpolator. The algorithm was implemented with the RBFinterpolator function in the Python language *scipy* library (Peterson et al. 2020) using a multiquadric kernel with parameter values *epsilon* = 0.1 and *smoothing*=0.001. This initial step matched the landmarks of the template to the corresponding locations on the target ear within 0.01 mm while smoothly morphing the geometry between the landmarks.

After manual landmarking, the fine fitting of the template to the target was accomplished fully automatically using an iterative algorithm implemented in Python. At each iteration, a set of 8000 vertices were randomly selected on the template along with the 2000 vertices currently having the largest distance from the target. For each of the source vertices, a "close" vertex on the target was sought, subject to weighting and distance filtering criteria. Specifically, the search radius was limited to 3 mm and the discrepancy in the direction of the normal at the source and target points was penalized, so that points

with similar normal were favored. A multiquadric RBF morph was performed using the manually and automatically defined landmarks used in the first step, as well as the ~10k template vertices for which target points were identified. This “normal aware” fine fitting enabled the thin areas of the pinna to be fit accurately and helped to maximize homology along the areas of high curvature on the helix and antihelix. After some experimentation, four iterations of this process were applied to each ear.

The distances between the fitted template and the target at each template vertex were computed to assess the goodness of fit. The median of the median fit discrepancies across ears was 0.03 mm, with a median 99.9th-percentile value of 0.44 mm, which is less than the original CT scan resolution. Most of the fit discrepancies larger than 0.5 mm were in the area of the ear lobe and none was in the concha or canal areas.

Statistical Analysis

A principal component analysis was conducted on the coordinates of the fitted template vertices. The coordinates for each ear were flattened into a single vector, concatenated row-wise with the data from the other ears, and a singular value decomposition was computed on this matrix using *scipy.linalg.svd* (Peterson et al. 2020). The 331 resulting eigenvalues and eigenvectors were retained for analysis. To quantify the effects of condition variables and covariates, linear regression analyses were conducted predicting principal component scores from variables including sex, stature, body mass index, ear side (left/right), and patient posture (prone/supine). The predicted scores were used to reconstruct ear geometry.

RESULTS

Mean Ear

Figure 5 shows the mean ear from several angles. The high level of homology is evident in the crispness of the features on the helix and antihelix, and the first and second bend of the canal are readily evident.

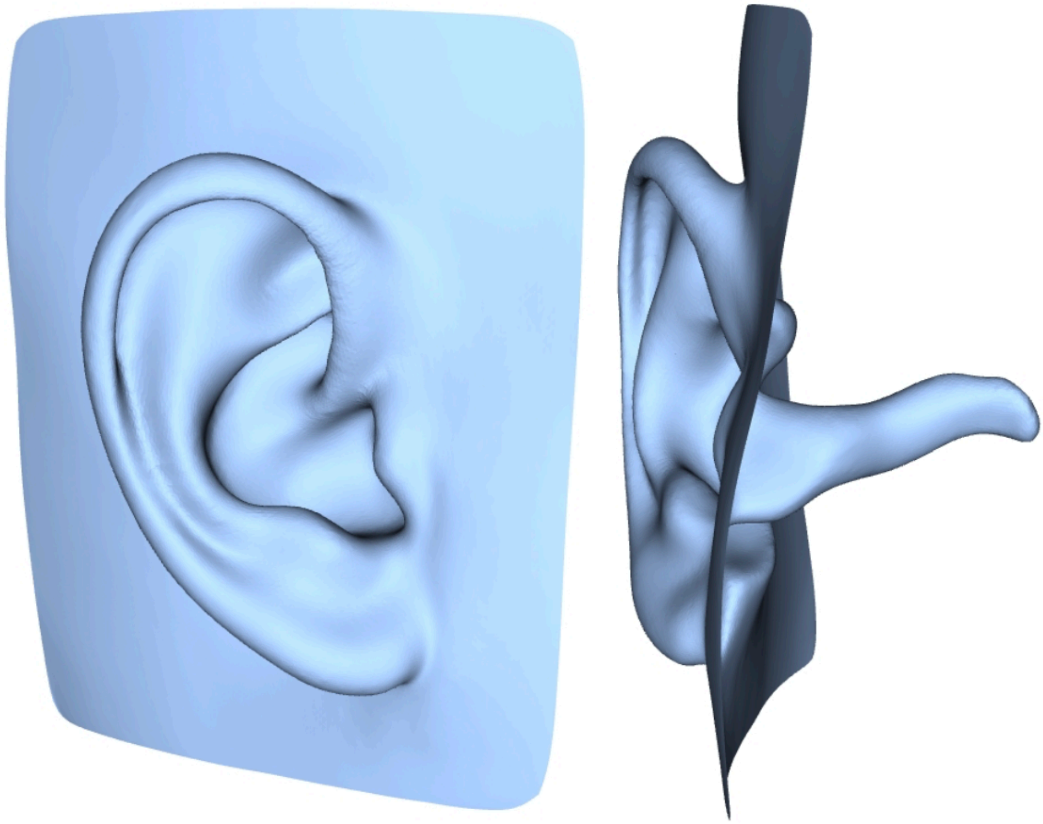

Figure 5a. Multiple views of the mean ear (N=331) with flat shading to show the polygon resolution.

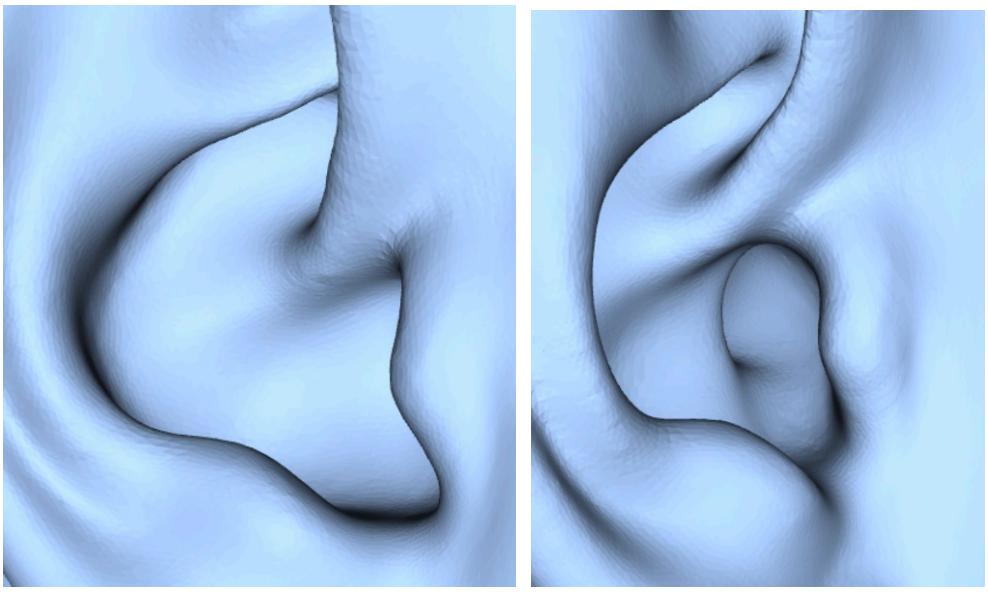

Figure 5b. Multiple views of the mean ear (N=331) with flat shading to show the polygon resolution.

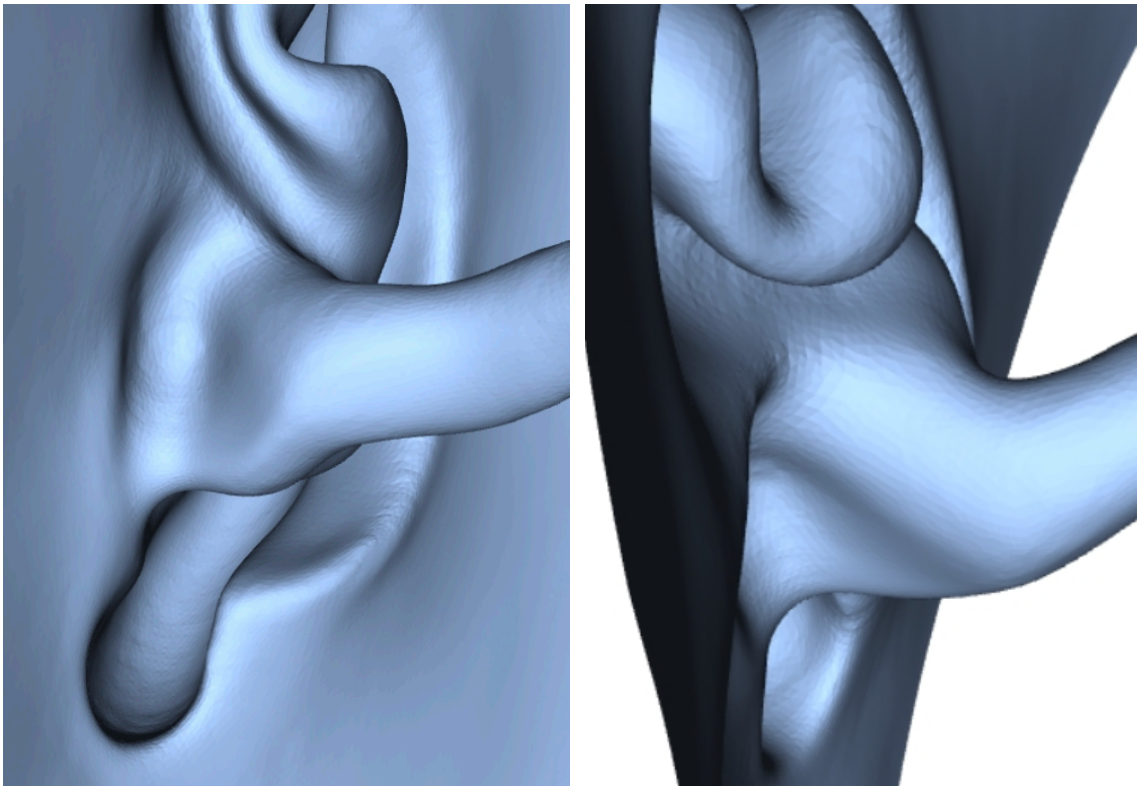

Figure 5c. Multiple views of the mean ear (N=331) with flat shading to show the polygon resolution.

Visualizing Principal Components

Figure 6 illustrates the first 8 principal components using ears generated by manipulating each PC by ±3 SD while holding the others at zero (the mean). The primary modes of variance are related to the position and orientation of the ear with respect to the skull (i.e., with respect to the coordinate system). The first PC is strongly related to the lateral position of the ear and hence to head breadth. A relatively clear relationship with local ear size is not seen until PC4. In interpreting Figure 5, consider that the PCA is partitioning variance in the vertex coordinates, and a large number of vertices are on the scalp portion of the model (approximately 25000 in the scalp, 28000 in the pinna, and 7000 in the canal beyond the first bend). Hence the lateral position of the ear (including the scalp) represents a large amount of variance, allowing PC1 to account for nearly half of the total. Figure 5 shows that the first 8 PCs account for about 91% of the variance in the model; 14 PCs are necessary to reach 95% of variance. Note, however, that considerable variation of interest for particular design problem could be associated with higher PCs.

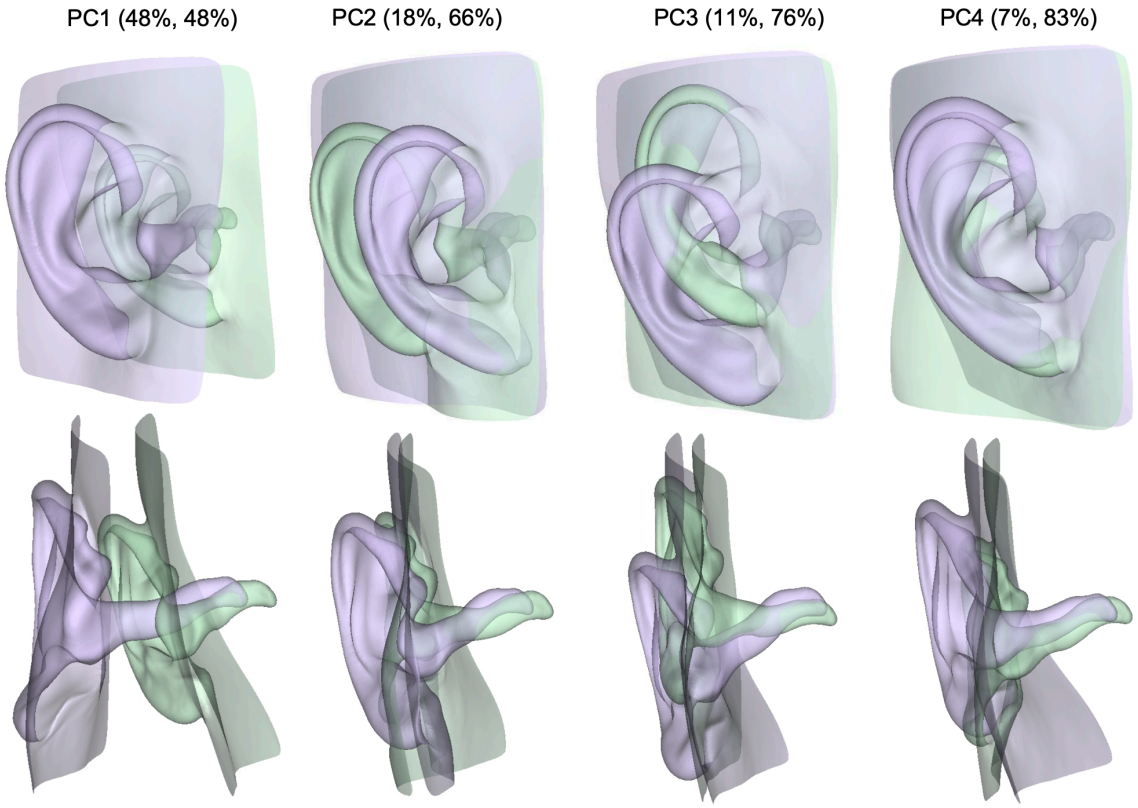

Figure 6A. Illustrations of the first 4 modes of variance (principal components) obtained by varying each PC by ±3 standard deviations while holding the others at zero (i.e., the mean). The numbers above each figure are the percentage of variance accounted for by the PC and the cumulative variance including that PC and all lower numbered PCs. The colors are arbitrary, representing the extremes of each component. Note that the sign of each component is also arbitrary.

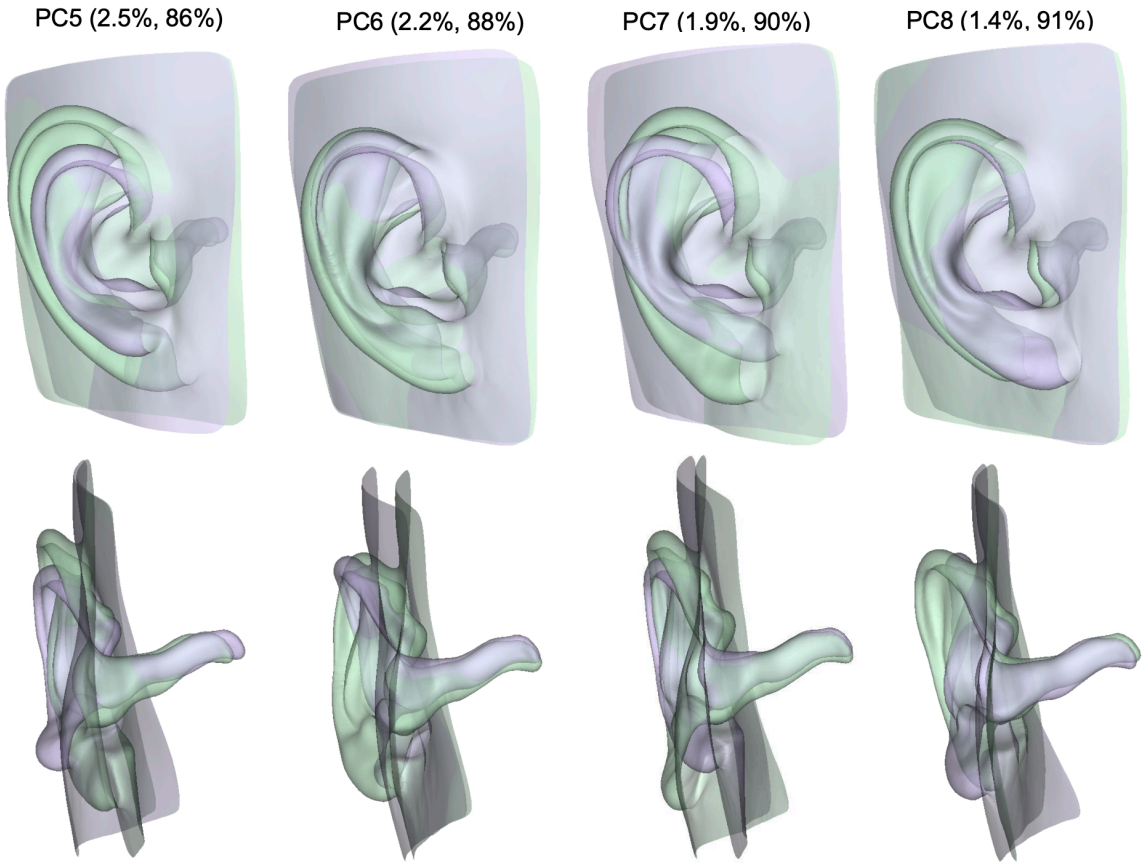

Figure 6B. Illustrations of the 5th through 8th modes of variance (principal components) obtained by varying each PC by ±3 standard deviations while holding the others at zero (i.e., the mean). The numbers above each figure are the percentage of variance accounted for by the PC and the cumulative variance including that PC and all lower numbered PCs. The colors are arbitrary, representing the extremes of each component. Note that the sign of each component is also arbitrary.

Effects of Covariates

The relationship between ear size, shape, and position in relation to covariates was examined using linear regression predicting PC scores. All PCs were retained for this analysis, so the results are mathematically equivalent to predicting vertex coordinates directly.

Figure 7 compares the mean prone and supine ears. The supine ear lies slightly rearward of the prone ear, relative to the skull, consistent with the effects of gravity on the ear and adjacent soft tissue. In the analysis below, this effect is neglected; because approximately equal numbers of prone and supine ears this effect is minimized.

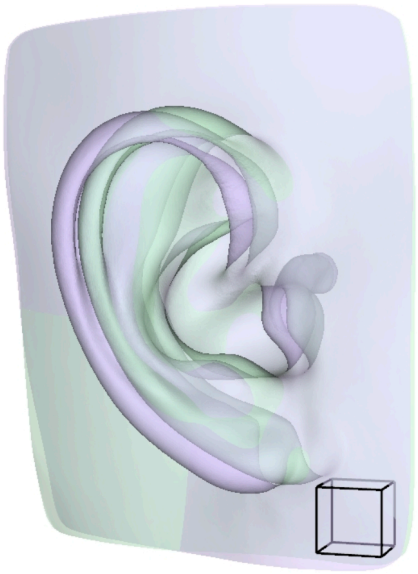

Figure 7. Mean ears from prone (green) vs supine (purple) postures. All ears are represented in skull-based coordinates, so the difference in fore-aft position of approximately 4 mm represents the opposite effects of gravity on soft tissue movement relative to the skull in the two postures. Wireframe cube has 10-mm edge length and is aligned to the head coordinate system.

Figure 8 shows the mean male and female ears, without adjusting for any other covariates. As expected, the ears have visually similar shape, but the female ear is smaller and angled out slightly more at the top. Figure 9 shows the effects of age for male and female ears, demonstrating a large effect of age on ear size and a small effect on fore-aft position. The male effect of age on size is slightly larger, and the ears shift rearward more with age for men than for women.

The effect of stature and BMI within sex are shown in Figure 10. Stature was varied from the 5th percentile to 95th percentile values for the US population (1627 to 1870 mm for men and 1500 to 1750 mm for women) and BMI was varied using the same values for both sexes (22 to 40 kg/m^2). Stature, a surrogate for overall body size, has a similar effect for both men and women. BMI has a surprisingly large association with the lateral position and angle of the lower portion of the ear, consistent with the ear canal being stretched over time as the soft tissue accumulates in the area. The effects are similar for men and women.

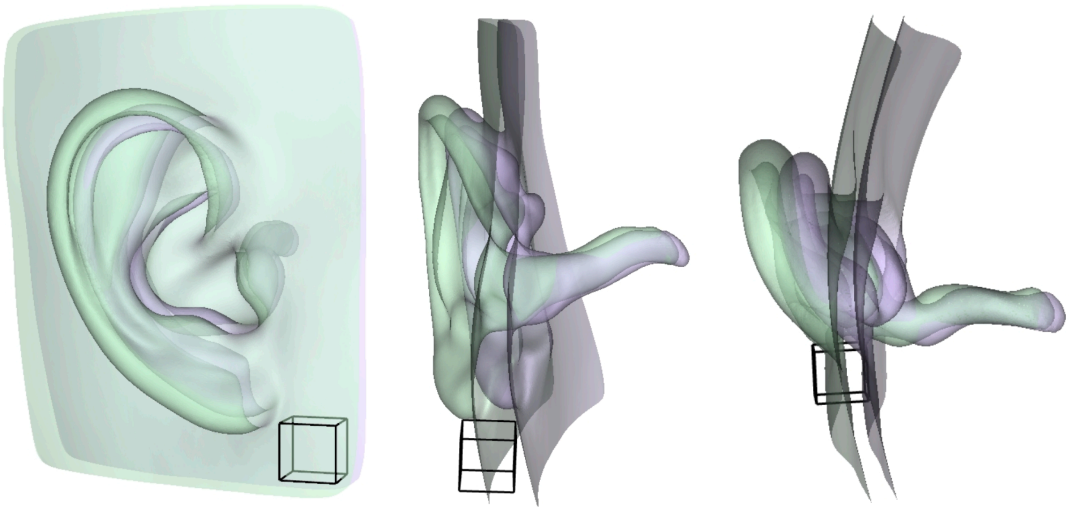

Figure 8. Mean male (green) and female (purple) ears. Wireframe cube has 10-mm edge length and is aligned to the head coordinate system.

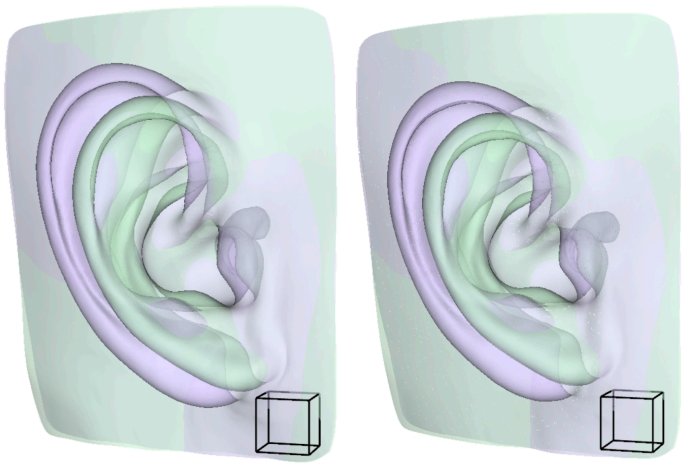

Figure 9. Effect of age for male (left) and female (right). Older ears (purple) are larger. Wireframe cube has 10-mm edge length and is aligned to the head coordinate system.

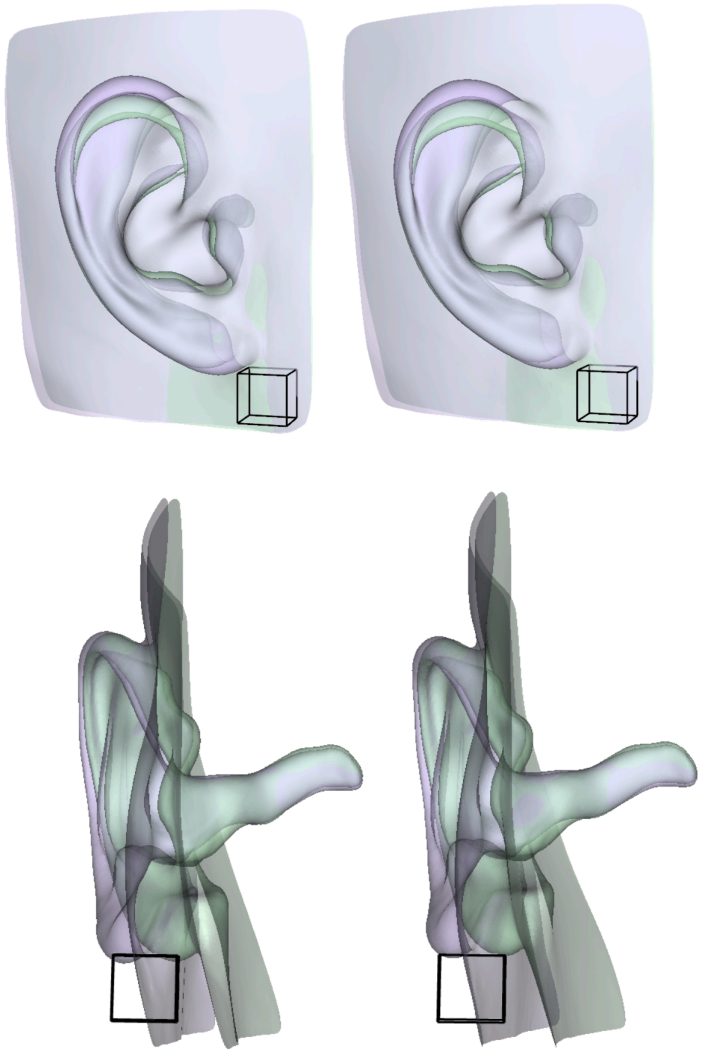

Figure 10. Top: Illustrations of the effects of stature (5^{th} to 95^{th} percentile within sex, and bottom: BMI (22 to 40 kg/m^2); male left, female right.

PCA on the Pinna

For some applications, an analysis local to the pinna may be more useful than preceding analysis in head coordinates. Figure 11 shows the results of PCA on points in the pinna and the outer area of the canal. The analysis was conducted after translating the tragion location on each ear to the origin.

In this case, the first PC is strongly related to the overall size of the pinna, while the second is related to the front-view angle. The ear rotation in sagittal view is associated with PC4.

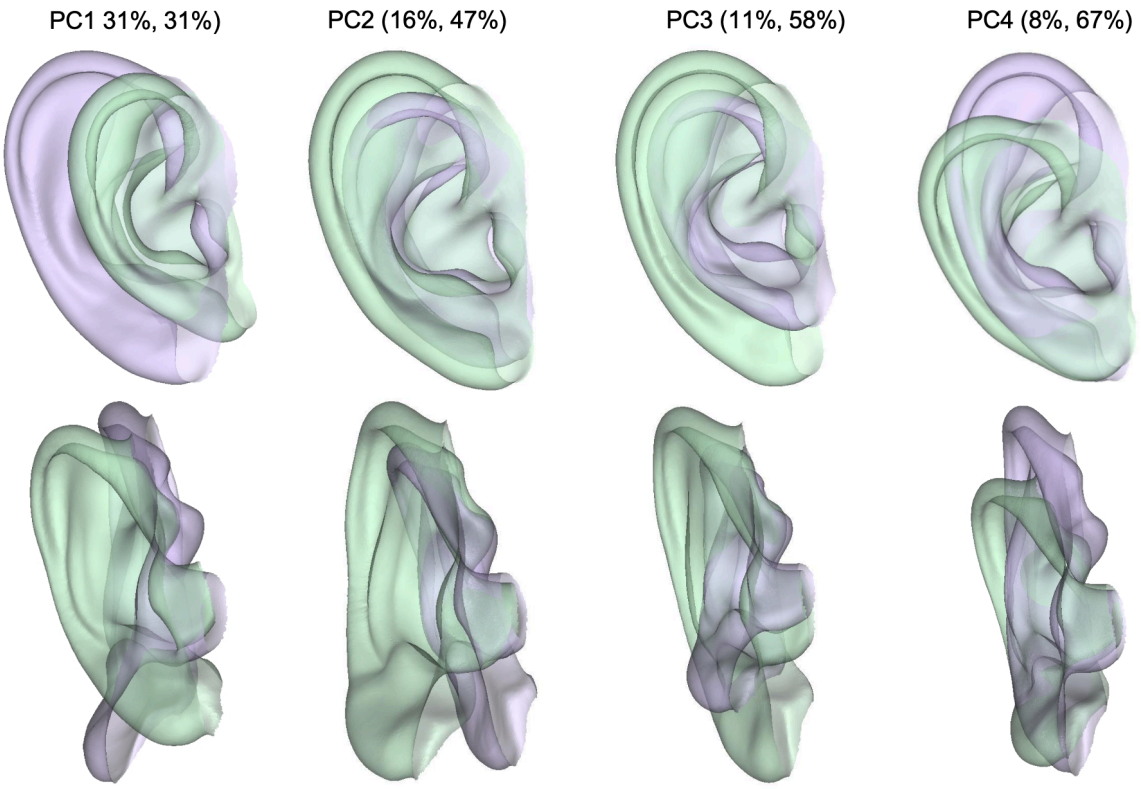

Figure 11A. Illustrations of the first 4 modes of variance (principal components) **of the pinna** obtained by varying each PC by ±3 standard deviations while holding the others at zero (i.e., the mean). The numbers above each figure are the percentage of variance accounted for by the PC and the cumulative variance including that PC and all lower numbered PCs.

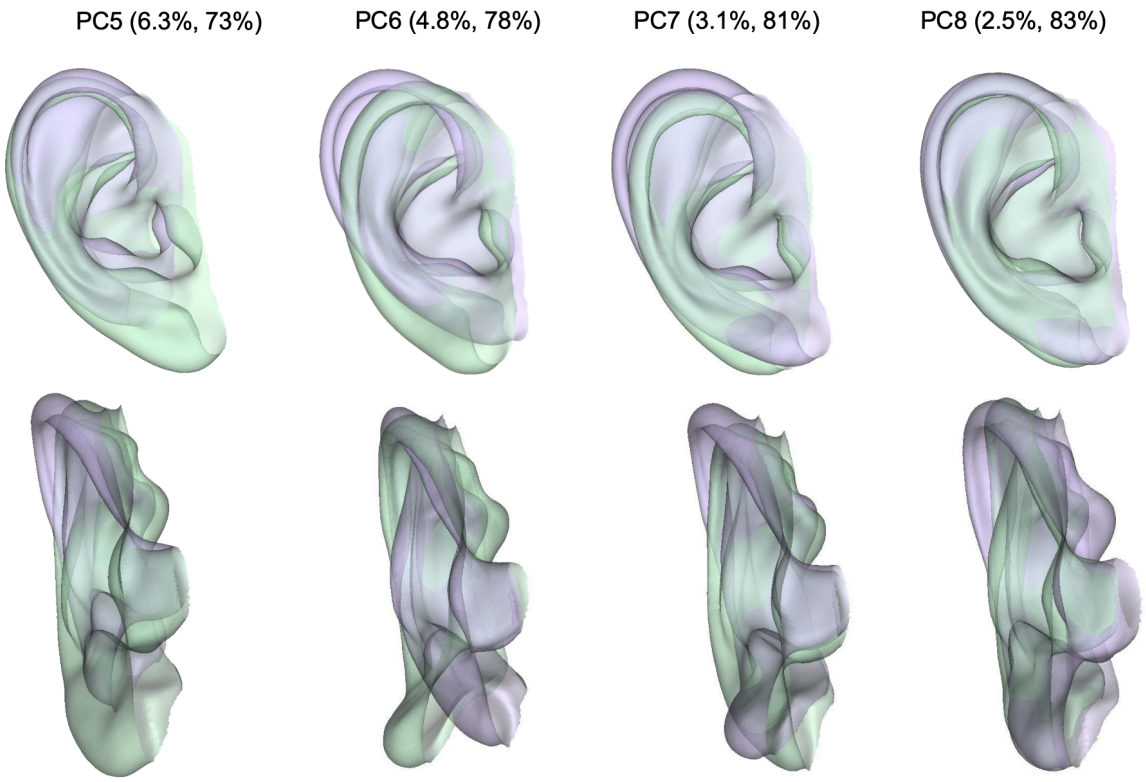

Figure 11B. Illustrations of the 5th through 8th modes of variance (principal components) **of the pinna** obtained by varying each PC by ±3 standard deviations while holding the others at zero (i.e., the mean). The numbers above each figure are the percentage of variance accounted for by the PC and the cumulative variance including that PC and all lower numbered PCs.

Effects of Covariates on the Pinna

Figures 12 through 14 show the association between covariates and the size and shape of the pinna. The male and female ears appear much more similar when the effect of head breadth is removed (compare with Figure 9). The effect of age is similar between the whole-ear and pinna models, as age primarily affects the dimensions of the pinna. The effects of stature and BMI in the pinnal model are also similar to the whole-ear model.

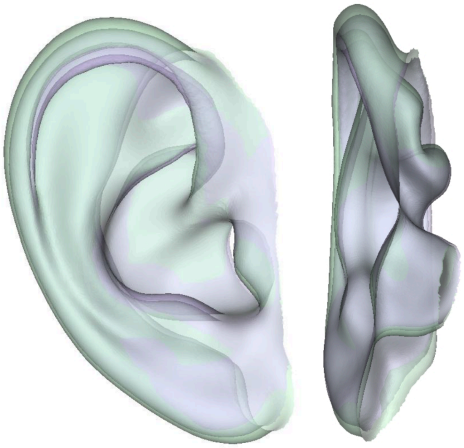

Figure 12. Mean male (green) and female (purple) pinnae.

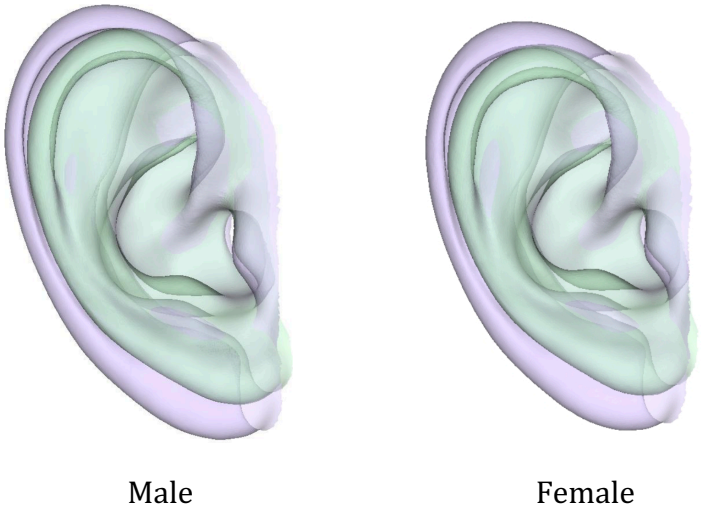

Figure 13. Effect of age for male (left) and female (right). Older ears (purple) are larger.

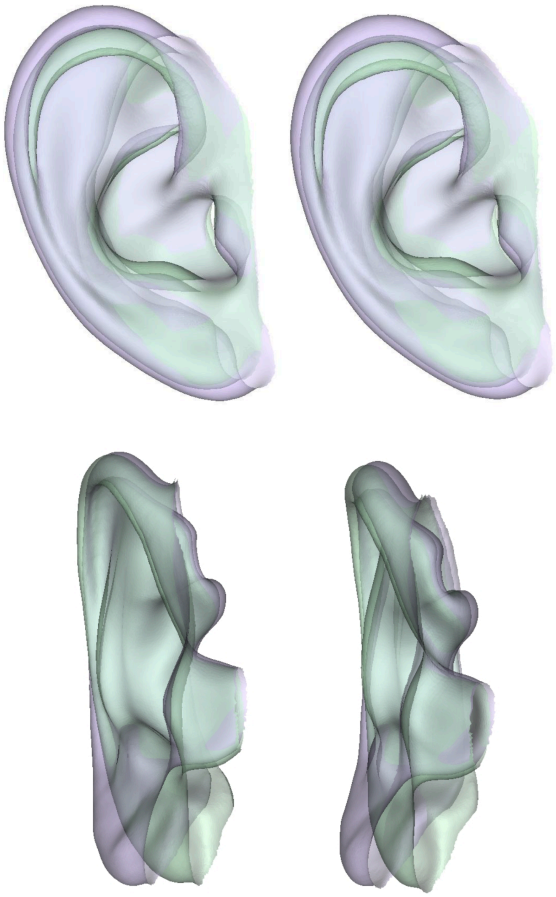

Figure 14. Top: Illustrations of the effects of stature (5^{th} to 95^{th} percentile within sex, and bottom: BMI (22 to 40 kg/m^2); male left, female right.

Generative Modeling for Design

For design evaluations, investigating the fit relative to all of the ears in the database may not be practical. Consequently, it may be valuable for some applications to have a smaller number of ears that represent a wide range of certain relevant characteristics. A boundary model approach in PCA space was applied in two coordinate systems. First, ears were generated in the space of the first three principal components relative to the skull coordinate system. These ears are particularly relevant to the design of over-ear devices, such as headphones. Under the assumption that disaccommodation could occur due to a device being either too small or too large for a particular ear feature, ears were generated that span 95% of the variance on the first three PCs. Referring to Figure 11, the first three PCs account for 76% of the total variance. Boundary ears were generated at the extremes of each axis on the 95% multinormal enclosure ellipsoid (6 ears) and at the 8 intermediate points on the boundary for a total of 14. Figure 15 shows these boundary ears relative to the mean ear and individually. The generated ears span a wide range of size, locations, and orientations in the head-centered coordinate system.

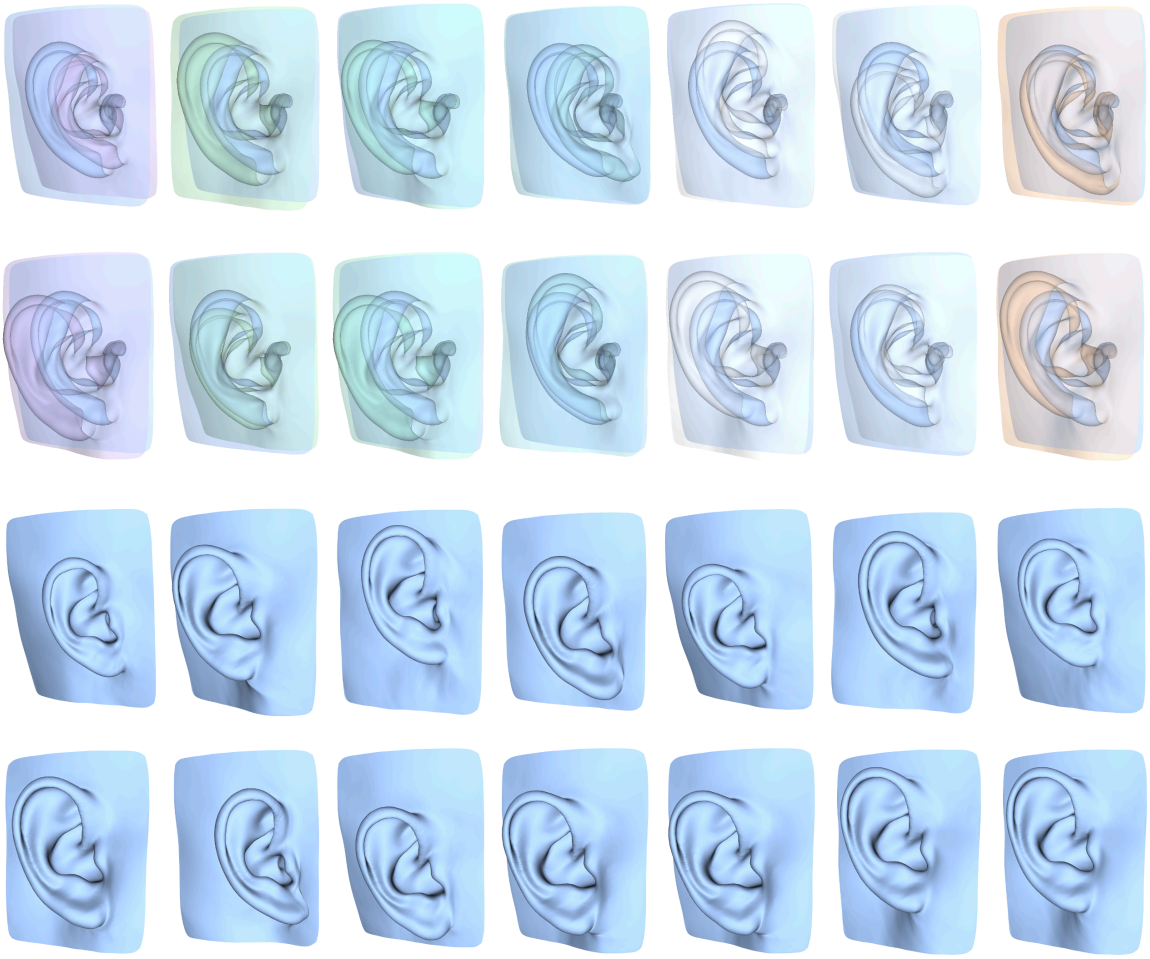

Figure 15. Boundary ears on first 3 PCs overlaid with the mean ear (top) and individually (bottom).

Figure 16 shows boundary ears computed in the same manner as those in Figure 15 for the PCA conducted on the pinna geometry centered at the tragion. Compared with the ears generated using the whole-ear model, these boundary ears are more relevant for the design and assessment of in-ear devices. In these representations, the variability in size and shape of the pinna is more evident, including readily apparent variation in the shape of the concha and tragal notch.

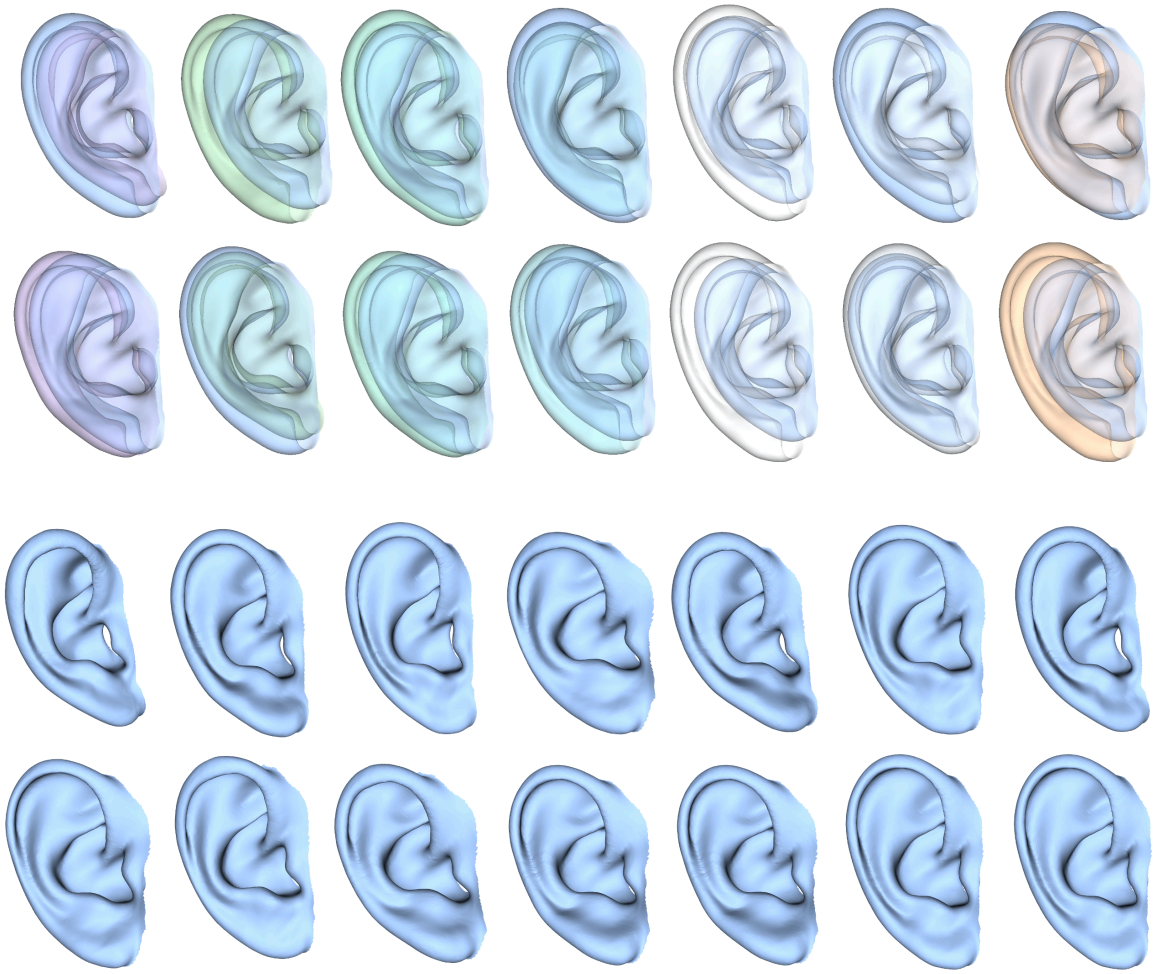

Figure 16. Boundary ears on first 3 PCs for the pinna overlaid with the mean ear (top) and individually (bottom).

Integrating Head and Ear

A preliminary effort was made to integrate the head-center ear model with UMTRI's whole-head surface model (Park et al. 2021). Generally, we would like to be able to create the most likely head for any ear and the most likely ear for any head, or alternatively to be able to explore the range of possible ear shapes for a given head and face. Currently, the only linkages between the two models are through the covariates (sex) and the location of ear landmarks. The male head model was reparameterized to predict the head based on the location of the tragion landmark as well as four landmarks on the perimeter of the pinna that are present in the head model. One challenge is that the head model is centered on the mid-point between the tragion landmarks, but the current study demonstrated that the tragion landmark is in a variable location with respect to the skull-based Frankfurt plane. Because all of the tragion landmarks in the head dataset have X and Z coordinates of zero, the ear data were first shifted to align the tragion with the XZ origin. Figure 17 shows some examples of heads predicted from the ear geometry

(i.e., pinna landmarks) of individual subjects. The range of face details is limited by the space of the male head model, which is based on 80 young men, but a surprisingly, a wide range of head and face shapes are created. This indicates relatively strong correlations between head/face shape and ear size, shape, and orientation. Some correlations are obvious: ears farther from the midline of the head indicate a larger head, with the associated characteristics. More research will be needed to develop a useful, integrated model based on this approach.

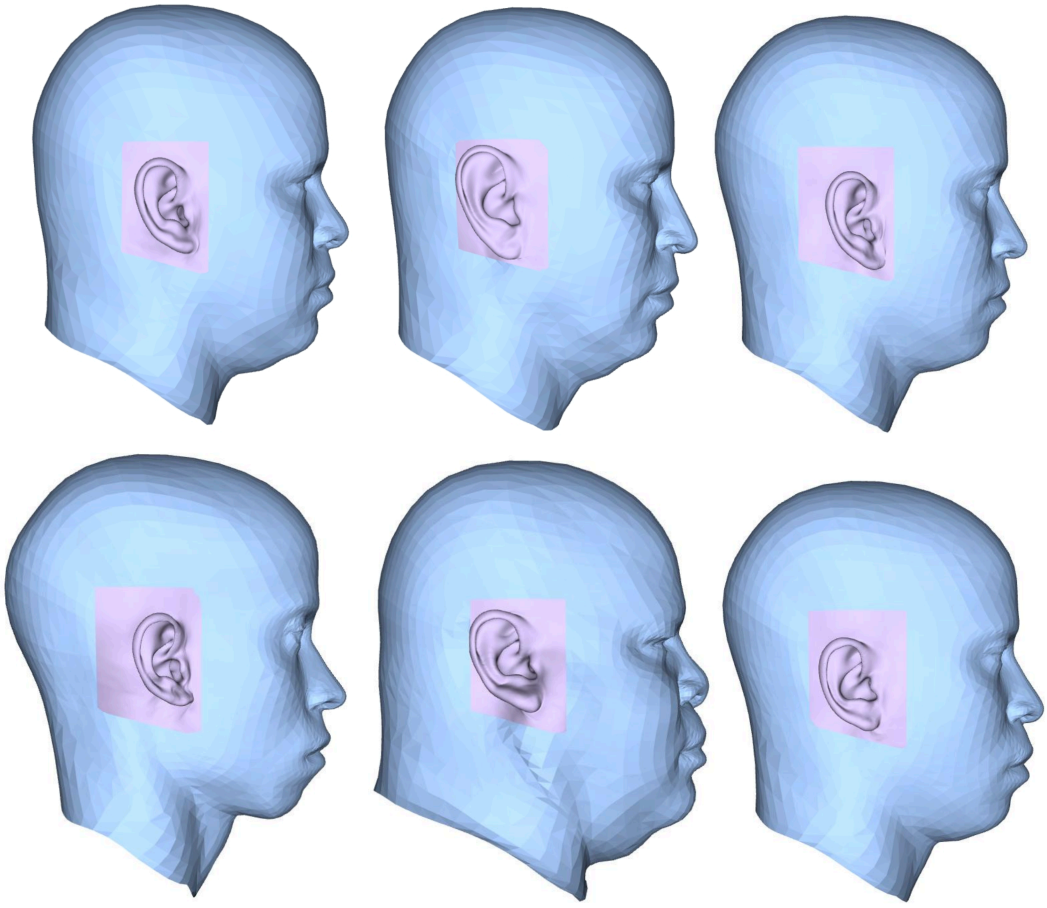

Figure 17. Illustration of outputs of preliminary effort to generate head/face shapes from ear geometry. The head and face are predicted from the 3D locations of 5 ear landmarks on ears extracted from 6 male subjects.

DISCUSSION

The dataset and statistical models presented here are novel in several important ways. This is the first reported dataset of pinna and canal geometry based on CT data and incorporates a larger sample size than previously published 3D ear datasets based on homologous template fitting. CT data has not been used for prospective studies because of the ethical concerns regarding exposure to radiation, but the retrospective nature of the current study using medically necessitated scans eliminates that concern. The use of CT allows the full canal to be included in the same model as the pinna. The resolution and accuracy are greater than typical of external optical scanners, and the fitting methodology resulted in high accuracy and good homology across the ear. The use of CT provides considerable advantages over the primary methods used in recent largescale studies that combined hand-held optical scanning with ear molding. Less manual manipulation of the data is needed, because the entire geometry is extracted in one pass, and hence the alignment of the pinna and canal data is not a concern.

This is also the first large-scale ear geometry dataset gathered in head-centered coordinates, which revealed a large amount of new information about the variance in ear position and orientation, including the large amount of variance in canal size, shape, and orientation relative to the temporal bone. The ability to express the ear geometry relative to the skull with high accuracy is another advantage of the CT-based technique. This analysis is the first to describe quantitatively the substantial effects of BMI on ear placement and orientation, suggesting that the ear canal is lengthened in individuals with higher BMI.

Boundary ear models potentially useful for design were generated in two coordinate systems, demonstrating the flexibility of the dataset. Many other analyses of ear regions could be conducted. For example, an analysis could focus exclusively on the concha and outer canal area to develop design targets for earbuds or hearing aids. Note that a PCA conducted on a small area can be used to generate whole ears consistent with the local targets.

The value of the homologous template fitting is emphasized by the nature of other recent publications, which have tabulated large numbers of dimensions based on manually extracted landmarks. With the current statistical model, any point-to-point dimensions can be extracted programmatically, replicating the prior work. But the 3D statistical models have far more value for use in 3D fitting trials. Reducing the 3D data to unidimensional information is effectively throwing away the most valuable part of the information to conform to outdated design practices that were developed before 3D information was available.

The study has limitations that may affect the applicability of the data. The sample size was smaller than originally intended. The original plan to sample both ears from 150 men and 150 women was difficult to implement due to the large percentage of CT studies with one or both ears deformed by postural supports. Further, the original plan contemplated simultaneously modeling the face, scalp, and ears, but the problems with face and scalp

deformation, along with incomplete data (for example, part of the face or back of the head missing) made it impractical to do that within the scope of the current study).

Although approximately equal numbers of male and female ears were analyzed, and a wide range of adult ages was represented, the distribution of geographical region of origin for the subjects is unknown. The population may not be representative of the U.S. population, which includes people with a wide range of regions of origin, although the large number of subjects obtained essentially at random from the radiology archives at a large U.S. teaching hospital suggests that the data will have broad utility. The distribution of available covariates (stature and BMI) closely match the range of the U.S. population. However, the sizes and shapes of ears from a different population could be different. Lee et al. 2018 showed small but systematic differences in linear dimensions between Korean and "Caucasian" populations. Utilizing these methods with CT studies from other populations would enable comparative studies. The statistical shape model developed in this work could also be used to fit 3D scan data from other studies, thereby putting all of the data into the same shape space.

The eardrum location could not be readily visualized in most of the scans, although as noted the ossicles were visible in some scans, enabling the development of a manual method for estimating the eardrum location based on the shape of the transition from the canal to middle ear. Although we were not able to systematically quantify this error, we estimate that the lateral position of the eardrum is typically within 2 mm of the manually identified location. The Poisson reconstruction used in the fitting process introduced a rounded inward end to the canal that is unrealistic; the base of this "bubble" is the estimated location of the ear drum. The ear location relative to the skull was slightly different in prone and supine poses, consistent with the action of gravity on the soft tissue. This effect was small compared with other aspects of variability and is effectively nulled out on the anterior-posterior axis by the use of approximately equal numbers of prone and supine scans. However, given the observed soft-tissue mobility, ear locations with the head upright may be slightly lower than those observed in these prone and supine scans. The ears used for this analysis were free of apparent pathology, but all individuals scanned were patients with a medically indicated need for a CT scan, and hence like any other patient population may not be fully representative of the general population.

The preliminary effort to integrate the ear model with a complete scalp and face model showed promising results. Modeling the tissue compliance would provide improved guidance for device design. Additional ears could be added to the database to improve the representation of unusual ear geometries. More focused analyses could be conducted on, for example, the canal only. The statistical model may also be useful for fitting sparse or noisy data obtained from other measurement modalities such as optical scanners and for imputing canal geometry from the size, shape, and location of the pinna.

REFERENCES

Alexander, K.S., Stott, D.J., Sivakumar, N.K. (2011). A morphometric study of the human ear. *Journal of Plastic, Reconstructive, and Aesthetic Surgery*, 64:41-47.

Baloch, S., Zouhar, A., and Fang, T. (2011). Deformable Registration of Organic Shapes via Surface Intrinsic Integrals: Application to Outer Ear Surfaces. In: Menze, B., Langs, G., Tu, Z., Criminisi, A. (eds) Medical Computer Vision. Recognition Techniques and Applications in Medical Imaging. MCV 2010. Lecture Notes in Computer Science, vol 6533. Springer, Berlin, Heidelberg. https://doi.org/10.1007/978-3-642-18421-5_2

Cintas, C., Quinto-Sánchez, M., Acuña, V., et al. (2017). Automatic ear detection and feature extraction using Geometric Morphometrics and convolutional neural networks. *IET Biometrics*. 6(3):221-233.

Chu, Y., Zhang, K., Wei, H., and Wang, Y. (2019). Template-based Ear Modeling and Reconstruction. *Proc. 2019 Chinese Automation Congress.*

Fantini, D., Avanzini, F., Ntalampiras, S., and Presti, G., HRTF Individualization Based on Anthropometric Measurements Extracted from 3D Head Meshes. 2021 Immersive and 3D (I3DA). 10.1109/I3DA48870.2021.961090

Farkas, LG. (1978). Anthropometry of normal and anomalous ears. Clinics in Plastic Surgery, 5(3):401-412.

Fernanda, A., Gentil, F., and Tavares, J. (2014) Segmentation algorithms for ear image data towards biomechanical studies, Computer Methods in Biomechanics and Biomedical Engineering, 17:8, 888-904, DOI: 10.1080/10255842.2012.723700

Fan, H., Yu, S., Wang, M., Li, M., Chu, J., Yan, Y., & Harris-Adamson, C. (2021). Analysis of the external acoustic meatus for ergonomic design: part I–measurement of the external acoustic meatus using casting, scanning and rapid estimation approaches. Ergonomics, 64(5), 640-656.

Fan, H., Yu, S., Wang, M., Li, M., Zhao, X., Ren, Y., & Harris Adamson, C. (2021). Analysis of the external acoustic meatus for ergonomic design: part II–anthropometric variations of the external acoustic meatus by sex, age and side in Chinese population. Ergonomics, 64(5), 657-670.

Fu, F., and Luximon, Y. (2020). A systematic review on ear anthropometry and its industrial design applications. Human Factors in Manufacturing, 30:176-194.

Ji, X., Zhu, Z., Gao, Z., Bai, X, and Hu, G. (2018). Anthropometry and classification of auricular concha for the ergonomic design of earphones. *Human Factors in Manufacturing*, 28:90-99.

Kamboj, A., Rani, R., and Nigam, A. (2020). A comprehensive survey and deep learning-based approach for human recognition using ear biometric. *The Visual Computer*. 38:2383-2416.

Lee, W., Yang, X., Jung, H., Bok, I., Kim, C., Kwon, O, and Heecheon, Y. (2018) Anthropometric analysis of 3D ear scans of Koreans and Caucasians for ear product design, *Ergonomics*, 61:11, 1480-1495, DOI: 10.1080/00140139.2018.1493150

Liu, B-S. (2008). Incorporating anthropometry into design of ear-related products. *Applied Ergonomics*, 39 (2008) 115–121.

Lu, P., Tsao, L., Yu, C., and Ma., L. (2021). Survey of ear anthropometry for young college students in China and its implications for ear‐related product design. Human Factors in Manufacturing, 31:86-97. Muntoni, A., and Cignoni, P. (2021). PyMeshLab. *Zenodo,* 10.5281/zenodo.4438750

Musy, M. et al., (2023) *vedo*, a python module for scientific analysis and visualization of 3D objects and point clouds, *Zenodo*, 10.5281/zenodo.7019968.

Niemitz, C., Nibbrig, M., and Zacher,V., (2007). Human ears grow throughout the entire lifetime according to complicated and sexually dimorphic patterns — conclusions from a cross-sectional analysis. Anthropologischer Anzeiger, 65(4):391-413.

Park, B-K., Corner, B.D., Hudson, J.A., Whitestone, J., Mullenger, C.R., and Reed, M.P. (2021). A three-dimensional parametric adult head model with representation of scalp shape variability under hair. *Applied Ergonomics*, 90: 103239

Paulsen, R., Larsen, R., Nielsen, C., Laugesen, S., and Ersboll, B. (2002). Building and Testing a Statistical Shape Model of the Human Ear Canal. In Doh and Kikinis (eds). of *Medical Image Computing and Computer Assisted Interventions* 2002, pp. 373–380, Springer, Berlin.

Peterson, W.W et al. and SciPy 1.0 Contributors. (2020) SciPy 1.0: Fundamental Algorithms for Scientific Computing in Python. *Nature Methods*, 17(3), 261-272.

Pollack, K., Majdak, P., and Furtades, H. (2020). A parametric pinna model for the calculations of head-related transfer functions. *Forum Acusticum*, Lyon, France. pp.1357-1360. 10.48465/fa.2020.0280.hal-03235345

Schroeder, W., Martin, K., and Lorensen, B. (2006). *The Visualization Toolkit (4th ed.)*, Kitware, ISBN 978-1-930934-19-1

Sforza, C., Grandi, G., Binelli, M., Tommasi, D.G., Rosati, R., and Ferrario, V.F. (2009). Age- and sex-related changes in the normal human ear. Forensic Science International, 187:110e1-110e7.

APPENDIX

Figure A1 shows a set of boundary ears generated from a PCA on the whole ear geometry after each ear was translated to place the tragion landmark at the origin. This presents a view of ear variability local to the ear that includes the adjacent scalp.

Figure A1. Boundary ears on first 3 PCs overlaid with the mean ear (top) and individually (bottom) for a PCA conducted in tragion-centered coordinates.